Geophysical Journal International

Geophys. J. Int. (2021) **225,** 1799–1811
GJI Gravity, Geodesy and Tides

doi: 10.1093/gji/ggab021

The ambiguous fault geometry derived from InSAR measurements of buried thrust earthquakes: a synthetic data based study

Yingfeng Zhang, Xinjian Shan, Wenyu Gong and Guohong Zhang

State Key Laboratory of Earthquake Dynamics, Institute of Geology, China Earthquake Administration, Beijing 100029*, China. E-mail: xjshan@ies.ac.cn*

Accepted 2021 January 11. Received 2021 January 5; in original form 2020 September 21

SUMMARY

The challenge of ruling out potential rupture nodal planes with opposite dip orientations during interferometric synthetic aperture radar (InSAR)-based kinematic inversions has been widely reported. Typically, slip on two or more different fault planes can match the surface deformation measurements equally well. The ambiguous choice of the nodal plane for the InSAR-based models was thought to be caused by InSAR's 1-D measurement and polar orbiting direction, leading to its poor sensitivity to north–south crustal motion. Through synthetic experiments and simulations, this paper quantitatively demonstrates the main reason of the ambiguous InSAR-based models, which confuse researchers in the small-to-moderate thrust earthquake cases investigation. We propose the inherent 1-D measurement is not the principle cause of the fault plane ambiguity, since models derived from the same InSAR data predict similar, but not identical, 3-D deformation patterns. They key to differentiating between these different models is to be able to resolve the small asymmetry in the surface deformation pattern, which may be smaller in amplitude than the typical noise levels in InSAR measurements. We investigate the fault geometry resolvability when using InSAR data with different noise levels through 'R' value. We find that the resolvability does not only rely on the InSAR noise, but also on the fault geometry itself (i.e. depth, dips angle and strike). Our result shows that it is impossible to uniquely determine the dip orientation of thrust earthquakes with $M_w < 6.0$ and depth > 5.0 km with InSAR data at a noise level that is typical for mountain belts. This inference is independent from the specific data set (i.e. interferogram or time-series) and allows one to assess if one can expect to be able to resolve the correct fault plane at all.

Key words: Satellite geodesy; Joint inversion; Seismicity and tectonics; Continental tectonics: compressional.

1 INTRODUCTION

Precise observations of surface deformation from interferometric synthetic aperture radar (InSAR) have led to major advances in our fundamental understanding of earthquake cycles and tectonic processes. InSAR data are able to provide remote measurements of ground displacements from crustal earthquakes of moderate size (M_w 5+) at high-spatial resolution (Elliott *et al.* 2016; He *et al.* 2020), and the number of earthquakes studied with this technique has exceeded 100 (Massonnet *et al.* 1994; Elliott *et al.* 2016). In particular, the launch of new InSAR satellites, together with open-source scientific inversion packages for data inversion (e.g. SDM, Wang *et al.* 2013) and powerful modern computers have dramatically increased its application to moderate/small earthquakes (M_w 5.0–M_w 6.5, e.g. Elliott *et al.* 2011; Daout *et al.* 2019, 2020; Gong *et al.* 2019; Zhang *et al.* 2020). The quality and regularity of new InSAR data means that the analysis of earthquakes from InSAR is becoming routine.

However, for the moderate/small earthquakes where fault slip is buried beneath the surface, the coseismic fault models derived from InSAR measurements frequently have large uncertainties in geometry, particularly in dip orientation (e.g. Lohman *et al.* 2002; Lohman & Barnhart 2010; Elliott *et al.* 2011; Gong *et al.* 2019; Zhang *et al.* 2020). In this study, we explore the causes of these uncertainties through experiments based on synthetic data.

Using the fault dip angle and corresponding InSAR fringe patterns, different thrust fault geometries can be sorted into two groups. The first group consists of blind thrust earthquakes with dip angles of 30–40°, which generate only one lobe of surface deformation measured by InSAR. These earthquakes are common in western China, for example: the 2008 M_w 6.3 Qaidam earthquake, the 2016 M_w 5.9 Menyuan earthquake and the 2016 M_w 6.3 Jinghe

earthquake (e.g. Elliott *et al.* 2011; Gong *et al.* 2019; Daout *et al.* 2020; Zhang *et al.* 2020; see Fig. 1). InSAR interferograms of such earthquakes can be modelled equally well by at least two fault sources with opposite dip orientations, even when multiple tracks with different line-of-sight (LOS) vectors are used in the inversion (Elliott *et al.* 2011; Gong *et al.* 2019; Daout *et al.* 2020; Zhang *et al.* 2020). The second group consists of thrust earthquakes with dip angles $<10^{\circ}$, that generate two lobes of deformation, which always have opposite sign, one of positive LOS and the other of negative LOS. That interferograms patterns could be generated by a pair of conjugate nodal planes since the subsidence signal moved from the footwall to the hanging wall (discussed in Sections 3.2 and 3.3). These low-angle thrust earthquakes typically concentrate along the collisional plate boundaries with contrasting rheology between the foreland and mountain range, for example: the 2016 M_w 6.3 Pishan earthquake, 2020 M_w 6.0 Kalpin earthquake and the 2019 M_w 5.4 Jammu earthquake in Pakistan (e.g. He *et al.* 2016; Ainscoe *et al.* 2017; Barnhart *et al.* 2018; see Fig. 1).

A number of different factors contribute to the fault plane geometry ambiguity, including: (1) the multiple noise sources, for example atmospheric artefacts, and contributions from inaccurate satellite orbit and auxiliary DEMs, (2) the InSAR observations only capturing the 1-D projection of 3-D surface deformation in the satellite's LOS and (3) the polar orbiting direction of the SAR satellite making it insensitive to north–south surface displacement (e.g. Lohman *et al.* 2002; Konca *et al.* 2019). For the east–west striking thrust faults common to the Alpine–Himalaya Belt, which generate predominantly vertical displacement and south–north shortening, these inherent shortcomings result in increased uncertainty in fault source parameters derived from InSAR measurements.

This study aims to provide a quantitative analysis of the ambiguities of source parameters derived from InSAR measurements, focusing particularly on thrust earthquakes with measurement noise and geometrical characteristics common to the border areas of Tibet and the Tian Shan. In Section 2, we describe the simulation methods and the features of atmospheric delay signals in our study region. In Section 3, we then show the effects of the fault geometry on the pattern and amplitudes of surface deformation, and resulting interferograms. We illustrate the underlying cause on the apparent dip orientation ambiguity in fault models derived from InSAR measurements through synthetic experiments. Finally, we map out the parameter domains in which we expect the fault geometry to not be uniquely determined by InSAR measurements of surface deformation, and finally discuss some solutions to solve these ambiguities in InSAR-based model parameters.

2 DATA AND METHODS

We synthetize surface deformation for a series of test earthquakes assuming that earthquake slip can be represented as a dislocation in an elastic half-space. We then combine the synthesized deformation with noise that resembles the statistical nature of the realistic data noise. These synthetic 'observations' are then used to explore what controls the ambiguity in fault geometry in kinematic fault slip inversions models.

2.1 Choice of study area

We selected two study areas: the Qilian Shan, Tian Shan Mountains and the southern Himalayas. These regions have hosted multiple thrust earthquakes studied by InSAR (e.g. 2008 M_w 6.3 Qaidam earthquake, 2016 M_w 5.9 Menyuan earthquake and 2017 M_w 6.3 Jinghe earthquake). Previous studies show an ambiguous choice of the nodal plane for these earthquakes (e.g. Elliott *et al.* 2011; Yu *et al.* 2018; Gong *et al.* 2019; Zhang *et al.* 2020).

2.2 Synthetic interferogram noise

The noise in InSAR interferograms mainly come from atmospheric retardation of radar waves, inaccuracies in the known position of the SAR satellite, residual topographic phase due to error in the DEM, noise due to variability in scattering, thermal noise at the pixel level and coregistration errors (Goldstein 1995; Zebker *et al.* 1997; Hanssen 1998). The noise due to interactions between the radar waves and the atmosphere are by far the largest of these signals. Therefore, to approximate realistic InSAR acquisition conditions, we used the regional and time specific noise, extracted from Generic Atmospheric Correction Online Service (GACOS) data in 2019, to analyse the impacts of the atmospheric delay signals on kinematic slip inversions in our study area.

We derived the atmospheric phase screen (APS) from GACOS data with a time interval of 6 d (the revisit time of Sentinel-1). Details of the APS pairs are shown in Table S3. The differential APS maps show strong spatial and temporal variation. In the spatial domain, the APSs are strongly correlated with the regional topography (Figs 2b and c). In the temporal domain, the unstable atmosphere in summer can enlarge the apparent LOS delays, producing much larger standard deviations of LOS delays than that in winter (Figs 2f and g). However, the delay signals still approximate a normal distribution with a zero mean over each year. The Stacking method (Biggs *et al.* 2007) have been found to significantly improve the signal quality (Fig. 2e).

Note that the atmospheric delay signals at our selected study areas (Tian Shan and North Qilian) are characterized with similar spatial patterns, but with variable amplitude (Figs S1, S2 and S3). We selected GACOS pairs with the largest, medium and smallest standard deviations, respectively, as the atmospheric noise that will be added into the synthetic earthquake deformations in the following sections. We did not project the GACOS APS products to the LOS of Sentinel-1, since we just need a noise source with realistic spatial pattern in our simulation, but not remove the atmospheric noise from observations using them.

We also added white noise with a standard deviation of 5 mm (corresponding to about 5.6 rad of C-band data), representing the decorrelation and processing errors. We did not consider the orbital path errors, as it usually shows smooth trends and can be removed during the data process or estimated during the coseismic model inversion (Massonnet & Feigl 1998; Biggs *et al.* 2007). We also neglected the DEM related errors as modern SAR satellites can almost perfectly control the vertical baseline (<100 m), which will lead to only $\sim$1–2 mm DEM related errors for the 30 m SRTM DEM data (Farr *et al.* 2007; Ferretti 2014).

2.3 Inversion methods

For the forward modelling of the earthquake co-seismic surface deformation signal, the rectangular deformation in an elastic half-space (Okada 1985) was used. The Poisson ratio used in our modelling is 0.25, based on crustal seismic velocities of $Vp = 6.0\,\mathrm{km\,s^{-1}}$, $Vs = 3.45\,\mathrm{km\,s^{-1}}$ and a density of $2780\,\mathrm{kg\,m^{-3}}$ (Steck *et al.* 2009).

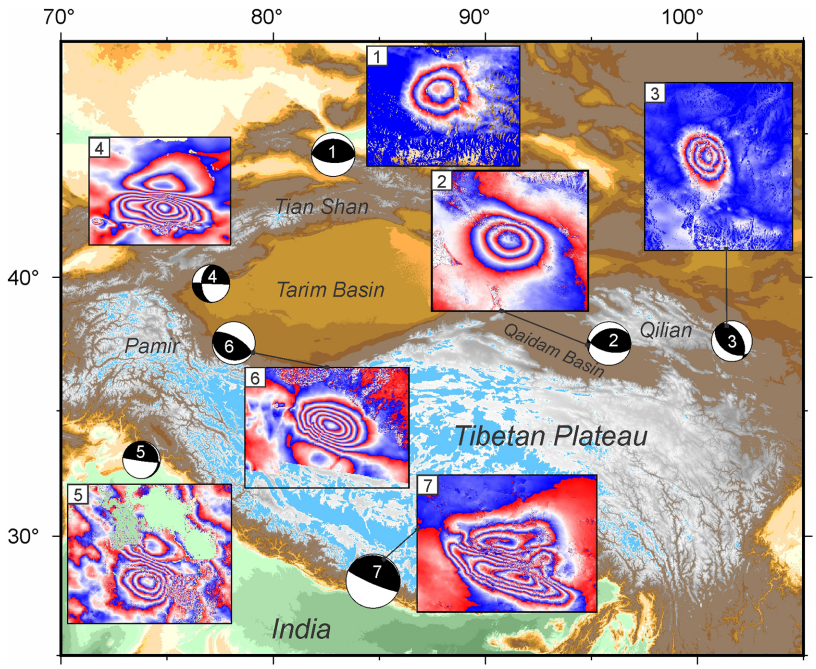

Figure 1. Wrapped interferograms of observed coseismic deformation around Tibetan Plateau discussed in this paper. 1. 2016 M_w 6.4 Jinghe earthquake (Gong *et al.* 2019); 2. 2008 M_w 6.3 Qaidam earthquake (Elliott *et al.* 2011); 3. 2016 M_w 5.9 Menyuan earthquake (Zhang *et al.* 2020); 4. 2020 M_w 6.0 Kalpin earthquake (Yao *et al.* 2020); 5. 2019 M_w 5.4 Jammu earthquake (Li *et al.* 2020); 6. 2016 M_w 6.4 Pishan earthquake (He *et al.* 2016); 7. 2015 M_w 7.9 Gorkha earthquake (Zhang *et al.* 2015). All interferograms (descending track) are directly taken from the citations in the brackets. The focal mechanisms can be found in Table S1.

The synthetic observations were generated by adding the forward model results to the noise described in Section 2.1.

During the inversion process, we presumed that earthquakes only ruptured a rectangular patch with uniform slip, which is a reasonable approximation for the moderate/small earthquakes we focus on in this study. A simulated annealing algorithm was used to search for the source fault geometry by minimizing the root-mean-square (RMS) misfit between model and synthetic observations (e.g. Copley 2015), and simultaneously estimate the possible linear ramp and constant offset, accounting for the remaining non-tectonic signals.

3 DIP AMBIGUITY FOR BURIED THRUST EARTHQUAKES

3.1 Thrust earthquake with one interferogram lobe

The interferograms of many buried thrust earthquakes are characterized by a single elliptical lobe of deformation (e.g. 1. Jinghe earthquake; 2. Qaidam earthquake; 3. Menyuan earthquake; Fig. 1). For these earthquakes, the fault strike and rake, but not dip, can typically be uniquely resolved (Elliott *et al.* 2011; Wang *et al.* 2017; Gong *et al.* 2019), as the wavelength and semi-major axis of the deformation pattern places constraints on the rupture depth and fault strike, but two fault planes with opposite dip orientations can account for the shape of the surface deformation (e.g. Lohman *et al.* 2002; Lohman & Barnhart 2010).

To explore the capability of InSAR data in resolving the correct fault plane for these thrust earthquakes, we calculated synthetic interferograms for both the ascending and descending tracks for a M_w 6.0 thrust earthquake with strike of 270°, dip of 35° and centroid depth of 9 km. The synthetic surface deformation pattern was then added into the synthetic noise (Fig. 2b). The noise-perturbed synthetic interferograms are used as data input for an inversion for source parameter estimates. The predefined parameter bounds are shown in Table S4, and the initial parameters were randomly generated within the bounds to run 800 groups of non-linear inversions to avoid the local minimum solutions in these highly non-linear inversions. The resulting solutions are presented as histograms in Fig. 3(g).

The result shows two peaks in the strike and dip panels that indicates the inversion found an ensemble of two possible kinematic models with opposite dip (Fig. 3g). Other parameters, such as the rupture depth and average slip, show a large range of possible solutions (Fig. 3). In spite of the uniform slip inversion, the two candidate models (N-dipping: strike/dip = 269/35; S-dipping: strike/dip = 83/54) fit the synthetic observations equally well (Figs 3c and f), indicating InSAR observations cannot identify the true model in this case.

We also used a layered model to perform the same experiment in this section, the process has been described in Supplementary Text S1. We found the effects from material heterogeneity in depth on our result is limited and will not change our conclusion (Fig. S7).

3.2 Thrust earthquakes with small dip angles (≤20°)

We simulated the interferograms of a M_w 6.3 synthetic thrust earthquake with strike of 270°, dip of 20° and superimpose upon this the medium level noise from around Kathmandu as the observation noise (Fig. S3b). We utilized the same inversion method in Section 3.1 to search the optimal geometries based on the synthetic InSAR data (Fig. 4a). The result shows two peaks with similar RMS

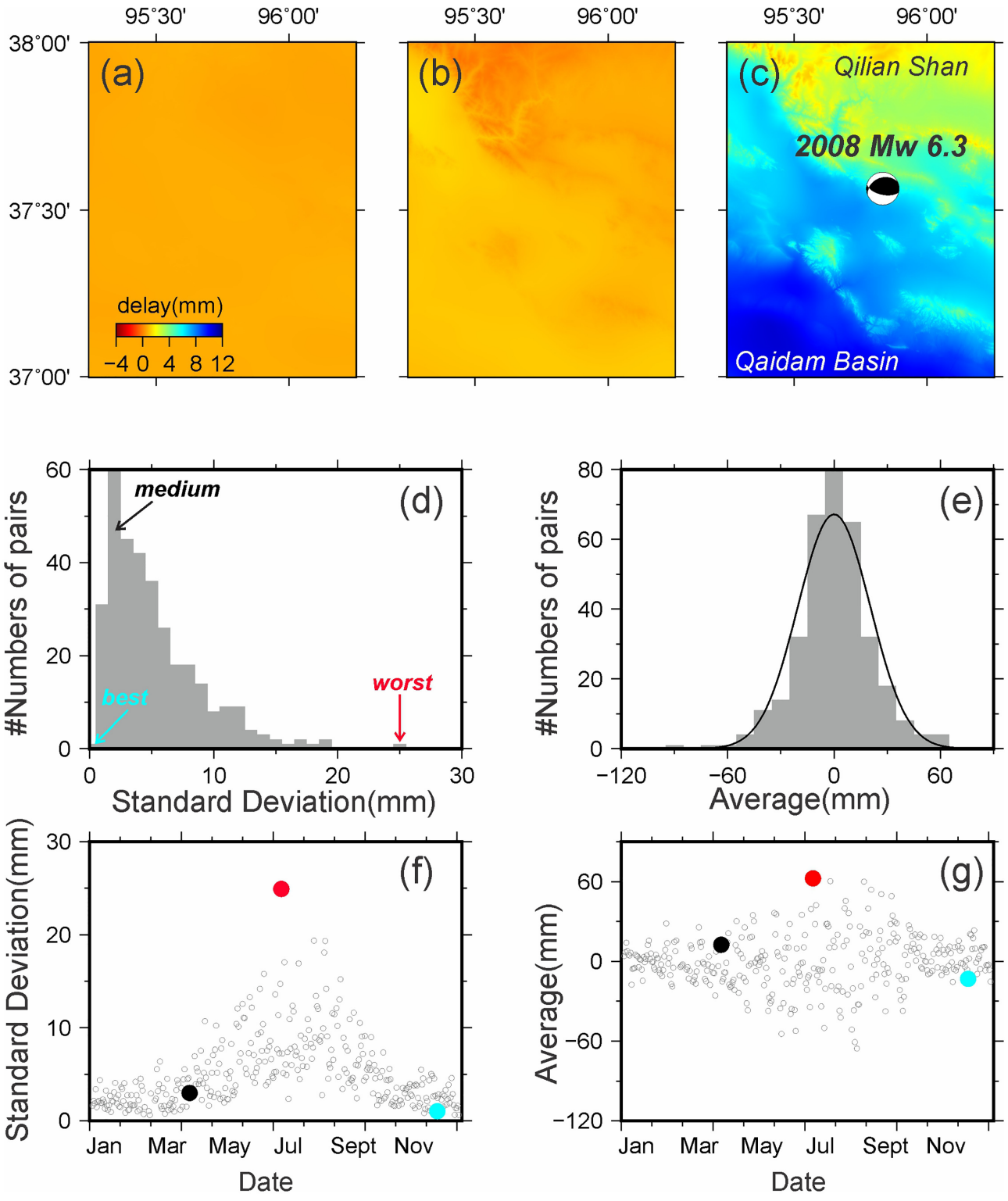

Figure 2. Spatial and temporal distributions of atmospheric delay signal in South Qilian Mountains. (a–c) Spatial pattern of the best (a), medium (b) and worst (c) scenario of atmospheric noise in 2019. (d–e) The standard deviation and average values distributions of the atmospheric noise. (f–g) the spatial standard deviation and mean temporal distribution in a year. The grey circles are the GACOS pairs, the red, black and blue dots mark the pairs with worst, medium and best atmospheric noise.

plotted for strike and dip in Figs 4(g) and (h), indicating a bimodal distribution of model parameters (N-dipping: strike/dip = 271/24; S-dipping: strike/dip = 90/67), which both can fit the InSAR observations equally well.

In general, the earthquakes with shallow dip angles, like 2016 M_w 6.4 Pishan, 2019 M_w 5.4 Jammu and 2020 M_w 6.0 Kalpin earthquake, can be explained by two conjugate nodal planes. One possible model is a thrust fault with high dip angle, and the

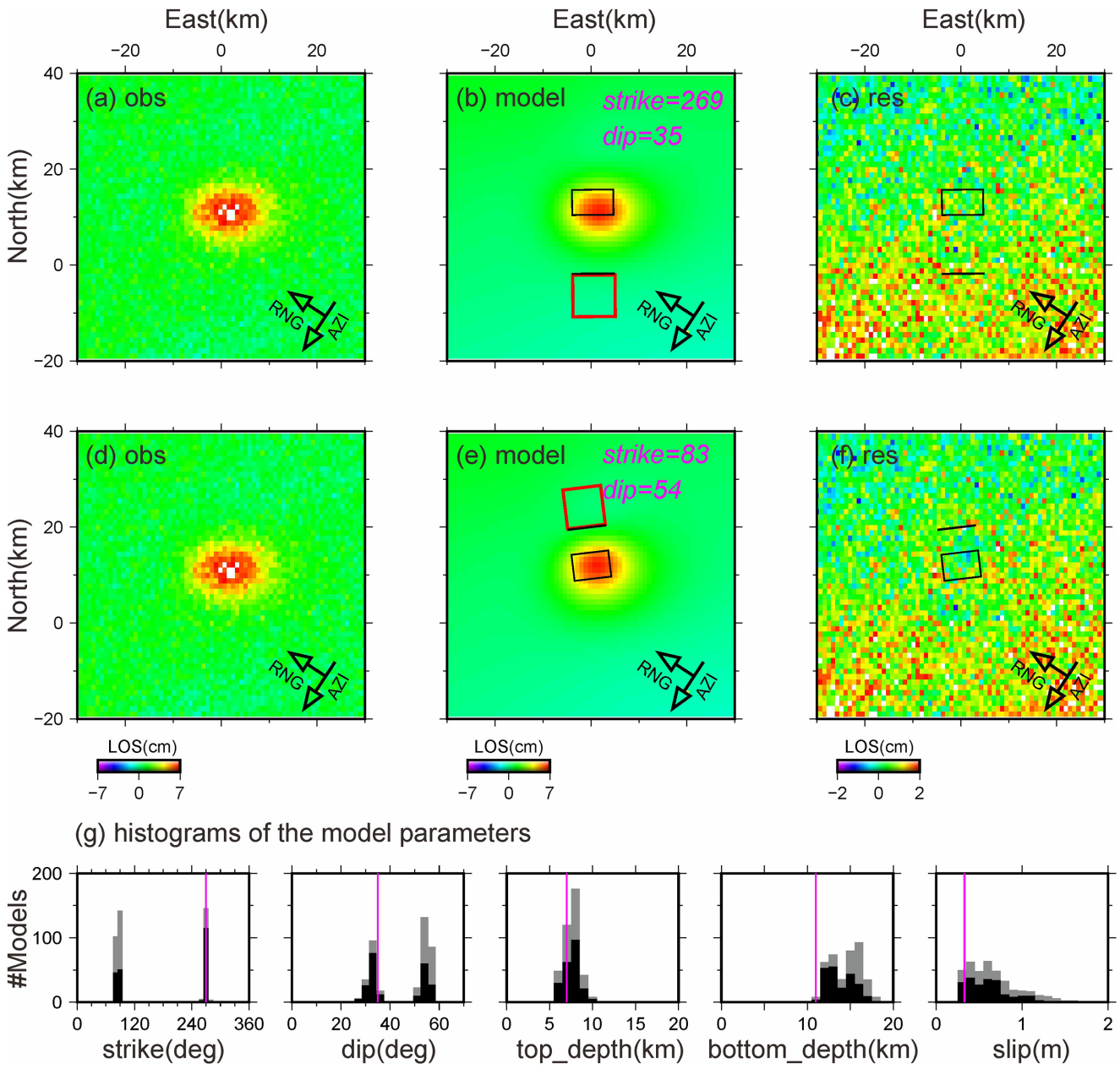

Figure 3. The synthetic observations, models and residuals derived from N-dipping (a–c) and S-dipping model (d–f) and (g) the histograms of strike, dip, depth and slip of the models that fit the data to within 25 per cent of the minimum misfit model (black) and 50 per cent of the minimum misfit model (grey). The red lines show the true value of the parameters. The black rectangular represent the surface projection of the source fault and the black straight lines are the corresponding fault traces. The red boxes outline the areas used to estimate average subsiding signals and signal-to-noise ratio (SNR) in Section 5. The fits for the ascending tracks are shown in Fig. S4.

corresponding fault trace extends between the uplift and subsidence. The other possibility is a thrust fault with low dip angle, and its fault trace could be at the outskirt of the deforming area, but close to the uplift zone as shown in this synthetic experiment.

3.3 Impacts of thrust fault dip and rupture depth on surface deformation

In the previous parts of this section, we demonstrated the ambiguity in driving fault dip from InSAR-derived surface deformation. In this section, we explore the causes of these ambiguities by examining the variation of the deformation pattern resulting from slip on a fault with various dip angles and centroid depth. We simulate a series of interferograms with fixed slip and geometry parameters (strike 270°, centroid depth 7.5 km, slip 0.5 m), while varying the dip angles. In this modelling experiment, the range of the dip angles was set to vary from 5° to 70° according to the observed earthquake dip distribution (Anderson 1951; Jackson & White 1989).

The resulting 2-D displacement profile across the fault centroid is shown in Figs 5(a) and (b). It shows that the asymmetry of the coseismic displacement increases with the lowering dip angle. The deformation caused by a steep fault tends to be symmetric, whereas the gently dipping fault plane makes the displacement

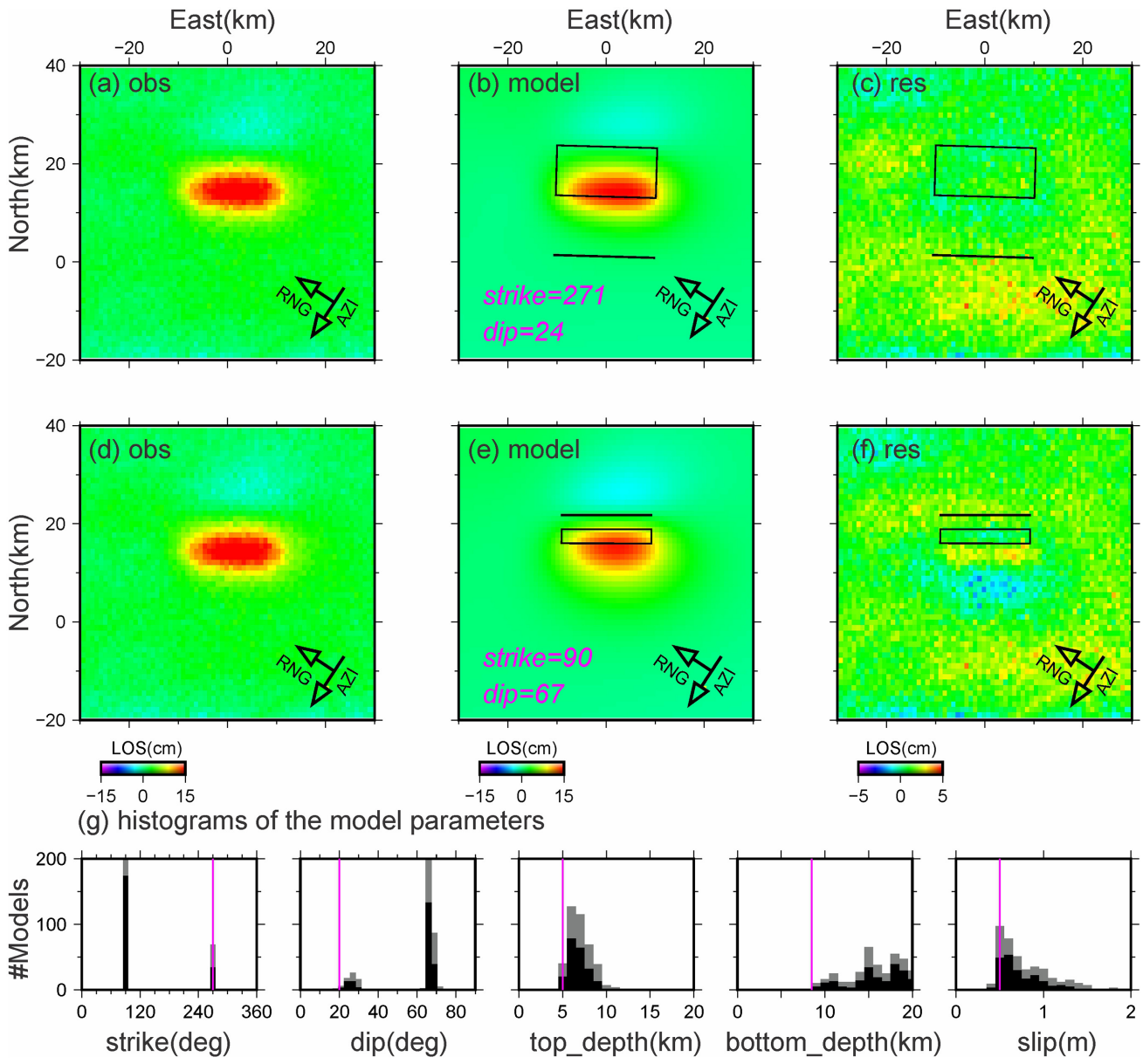

Figure 4. The synthetic observations, models and residuals derived from Model A (a–c) and Model B (d–f) in M_w 6.3 thrust earthquake with prominent single lobe of deformation. The fits to the ascending data are shown in Fig. S2. The rest of the caption is the same as in Fig. 3.

significantly asymmetric. Particularly for the thrust earthquake with dip angles of smaller than 30°, the subsidence on the footwall disappears and simultaneously a subsiding area appears on the hanging wall where the uplift would be in the cases with steep dip. This kind of deformation polarity reversal highlights the strong correlation between the dip angles to the surface deformation pattern.

Based on the same method used in the variable dip modelling, we simulated the interferograms caused by earthquakes with a variable rupture top-depth (from 3 to 15 km), fixed dip angle (30°) and magnitude (M_w 6.2). The resulting coseismic interferograms indicate the depth is strongly correlated with the deformation spatial wavelength (Figs 5c and d). The deeper centroid depth generates longer surface deformation wavelength, but smaller amplitude, which will probably make the subsidence zone on the footwall be buried into the background noise. Note that this is true only for the earthquakes with the similar dip and magnitude. Because the wavelength of the surface deformation is sensitive to the rupture depth, elastic dislocation modelling yields more accurate top and bottom depths of the earthquake faulting than seismology (Baumont *et al.* 2004; Bos *et al.* 2004; Dawson & Tregoning 2007).

The source fault ambiguity results from two features of the surface deformation pattern as fault dip and depth change: (1) the disappearance of subsidence in the footwall as the dip angle decreases and the depth increases and (2) the subsidence lobe moving to the hanging wall due to an unusual gentle dip angle.

In the first scenario, the appearance of the ambiguous models depends on the subsidence amplitude, which is affected by the dip angle, as well as the centroid depth for a specific magnitude. In the range of 30°–70°, the subsidence zone on the footwall will gradually

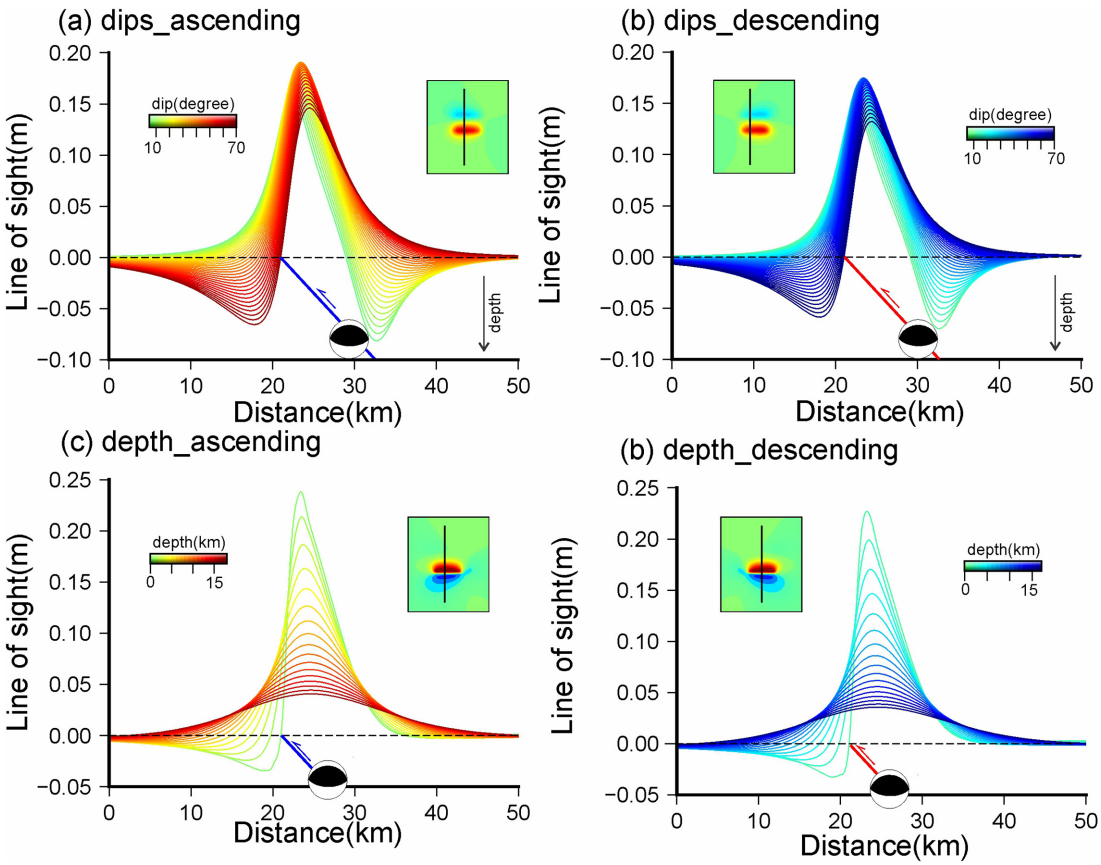

Figure 5. The forward coseismic deformation cross-section in in the satellite's line-of-sight (LOS) direction, using various dip angles (a), (b) and rupture top-depth (c), (d). The assumed rupture area is 10 × 17 km with average slip of 0.5 m,corresponding to M_w 6.2.

attenuate with decreasing dip angle, and eventually become invisible if the subsiding signals are close to the background noise level, leaving only an uplift lobe visible in the interferograms (e.g. 2008 M_w 6.3 Qaidam, 2016 M_w 6.3 Menyuan and 2017 M_w 6.4 Jinghe earthquake in Fig. 1). As revealed in Section 3.1, the source fault geometry cannot be determined uniquely just based on one lobe of deformation in the interferograms.

In intra-continental settings, the depth extent of seismicity is typically 5–20 km. Towards the top of this depth range, the subsidence lobe of a M_w 6.2 earthquake tends to disappear below the background noise, particularly the atmospheric delay in the interferograms (Figs 5c and d). In addition, the dip angles of thrust faults statistically concentrate in the range of 30°–60° (Sibson & Xie 1998; Middleton & Copley 2014), which gives rise to a relatively small subsiding signal on the footwall, probably at the same level with the background noise sometimes (Figs 5a and b). These two features of the typical seismogenic depth and thrust fault dip angles indicate that earthquakes with only one deformation lobe in the interferograms would frequently appear in nature, and therefore the ambiguous models could be more common than we expected before. Here we highlight that there could be a potential observational bias stemming from these modelling limitations in earthquake catalogues of the Alpine–Himalaya Belt constructed using automated processing and inversion of InSAR measurements.

The second scenario occurs for faults with a dip angle of <30°, where the subsidence lobe moves to the hanging wall, making it difficult to determine the location of the footwall, as we have shown in Section 3.2 (e.g. 2016 M_w 6.4 Pishan, 2019 M_w 5.4 Jammu and 2020 M_w 6.0 Kalpin earthquake in Fig. 1). These thrust earthquakes usually occur along foreland basin margins, where low-angle fault planes form along a weak layer between sediments and underthrusting interface (e.g. Ainscoe *et al.* 2017; Barnhart *et al.* 2018).

Researchers usually presume these earthquakes rupture fault planes with gentle dip angle dipping towards the mountains. As a result, this kind of ambiguity is rarely reported in the literature. This assumption is reasonable for the large earthquakes like 2015 M_w 7.9 Gorkha earthquake, but may not be true for the small earthquakes like 2019 M_w 5.4 Jammu earthquake, as they perhaps did not rupture the underthrusting interface between the mountains and foreland. We therefore have to carefully exam if it ruptured the gently dipping interface plane or a steep back thrust structure, which is important for understanding the regional tectonics and earthquake hazards.

4 3-D DEFORMATION FOR AMBIGUOUS MODELS

It is often stated that the 1-D measurement of LOS displacement from InSAR strongly limits the capability of this technique in the investigation of fault geometries (Wright *et al.* 2004; Feng & Jónsson 2012). In this section, we demonstrate that the 1-D measurements of InSAR is not the main cause of the apparent ambiguous

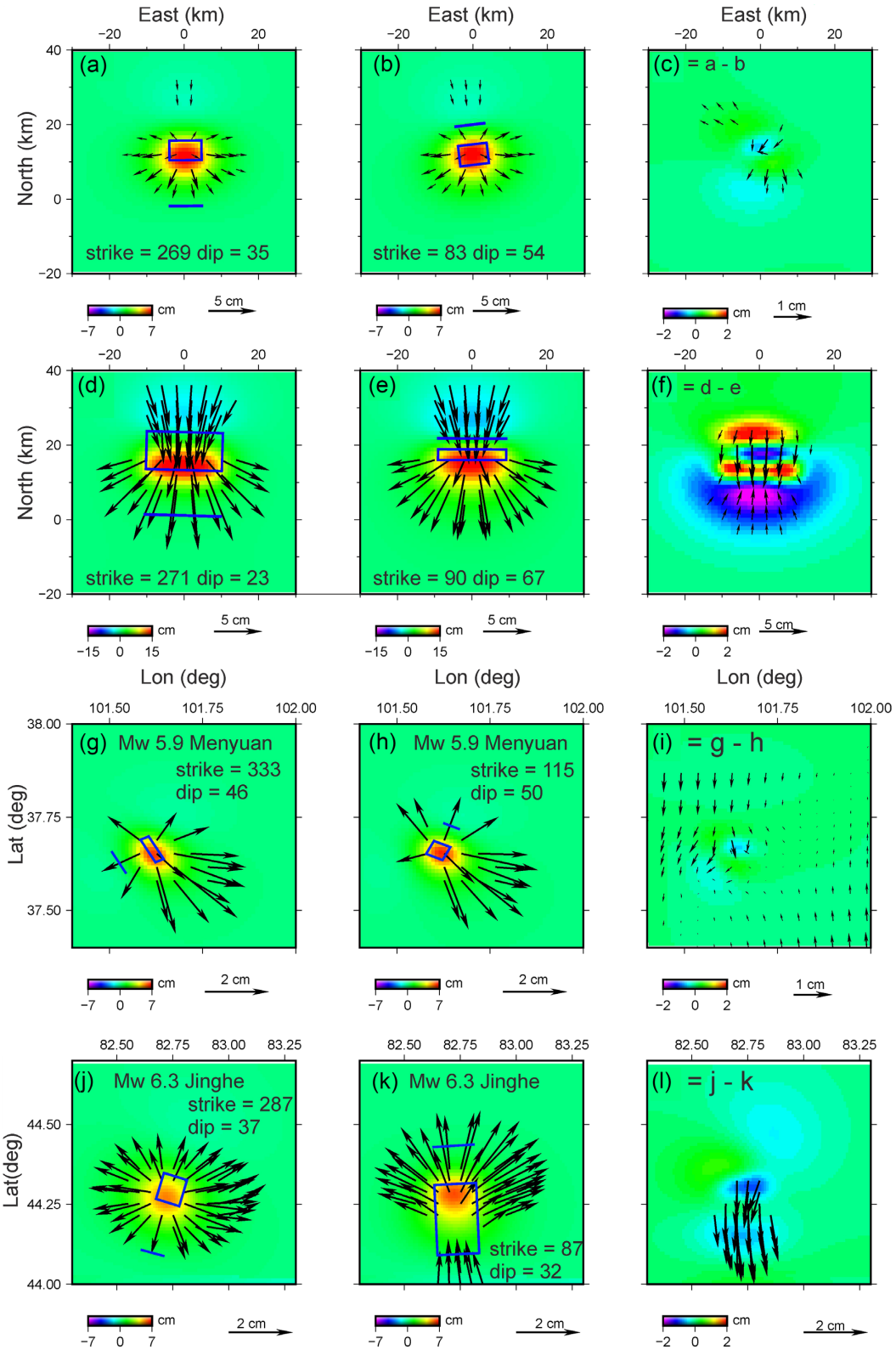

Figure 6. The forward modelling result based on the possible kinematic models resolved in the synthetic thrust earthquakes in Section 3.1 (a)–(c) thrust earthquakes in Section 3.2; (d)–(f) 2016 M_w 5.9 Menyuan earthquake (Zhang *et al.* 2020) and 2017 M_w 6.3 Jinghe earthquake (Gong *et al.* 2019). The colours present the vertical movements or their difference, and the black vectors show the corresponding horizontal movements.

models, especially for small-to-moderate thrust earthquakes. Fig. 6 shows the 3-D displacement filed calculated with the candidate fault models in Sections 3.1 and 3.2. Apart from the similarity in LOS (Figs 3 and 4), the two models with conjugate fault planes also generate similar deformation in the vertical and horizontal (Fig. 6). It is therefore difficult to determine the real source fault, even if Global Navigation Satellite System (GNSS) observations are available.

In practice, we sometimes have to face the apparent ambiguous models with conjugate fault planes, like the synthetic thrust earthquake in Figs 6(a) and (b). In these cases, the two candidate models can not only generate the same LOS displacements, but also the similar 3-D deformation with subtle differences, which makes it impossible to tell the true source fault model if the noise in the measurements is large. In the case of the M_w 5.9 Menyuan earthquake, the two candidate models correspond to the two nodal planes of its focal mechanisms constrained by teleseismic waveforms (Table S1; He *et al.* 2020), therefore seismology also cannot be used to differentiate between the candidate fault planes.

Fortunately, fault models derived from InSAR observations sometimes show two opposite dip orientations that are not conjugate to each other. For example, for the M_w 6.3 Jinghe earthquake, the candidate models predict significantly different horizontal displacements (Figs 6j and k), which means that GNSS observations can be used to determine the correct source fault. In comparison to the focal mechanisms, there is only one candidate fault plane consistent with the nodal plane determined from seismology. We can therefore determine the unique source fault model through applying multiple observations, such as GNSS, InSAR and teleseismic waveforms.

The helpless constrains of the GNSS data on dip orientation of those solutions with conjugate fault planes indicate those non-unique model solution does not simply result from the inherent 1-D observations of InSAR, at least it is not the principle cause. The key of InSAR to better constrain a unique model is if the background noise can be significantly removed to refine the deformation signals.

In this sense, the 1-D InSAR observations are equivalent to the 3D observations during the geodetic inversion. The 1-D LOS vector is a projection of 3-D displacements. This process will lead to a loss of the resolution of certain components of the deformation signal, especially for the N–S components (Wright *et al.* 2004). Given the dominating interferometric errors are additive signals, the composition of 1D LOS displacement in the end reduce the signal to noise ratio. In other word, the critical difference between GNSS and InSAR observation is the noise sensitivity of their components. For the cases in which the InSAR fails to resolve the dip orientation but GNSS measurements can, it is because the interferograms contain larger noise than GNSS and the small horizontal components of deformation projected into LOS are below the noise level, leading to the absence of the characteristic region of subsidence in the footwall.

In summary, the non-unique fault models derived from InSAR measurements are not directly caused by its 1-D measurement, but the non-deformation InSAR signals. The projection of 3-D signals to 1-D LOS deformation will reduce the ratio between deformation and noises, which further limits the recovery of fault parameters from inverting surface displacements, especially for the faults striking in E–W direction. Our analysis therefore suggests the increasing the signal to noise ratio will allow to solve the problems caused by the so-called 1-D measurements, including the ambiguous InSAR-derived model parameters.

5 THE GEOMETRIC PARAMETER SENSITIVITY OF THE AMBIGUOUS MODELS

Following the confirmation of these InSAR-based ambiguities, we now examine how the faulting parameters affect the unique determination of one of the fault plane from the inferred ensemble of ambiguous models. We used the empirical relations detailed in Supplementary Text S2 to generate synthetic earthquakes and then simulated Sentinel-1 interferograms ('signal' in eq. 1). The synthetic earthquake data set includes 200 000 earthquakes with magnitudes range from M_w 5.0 to 7.0. We ensured that all modelled earthquakes were not below the average seismogenic layer, which is 20 km in Qilian Shan and Qaidam Basin (Wei *et al.* 2010; Sloan *et al.* 2011). The atmospheric noise and white noise introduced in Section 2.1 were added into the synthetic interferograms as the observation noise ('noise in eq. 1).

The ambiguity of choice between nodal planes is caused by the masking of the subsidence signal in the footwall by noise. We therefore determine the resolvability of the correct model from the ambiguous choice of models by looking at the ratio:

$$R = \frac{\text{observation}}{|\text{noise}|} = \frac{\text{signal} + \text{noise}}{|\text{noise}|} = \begin{cases} 1 + \dfrac{\text{signal}}{\text{noise}}, (\text{noise} > 0) \\ -1 + \dfrac{\text{signal}}{\text{noise}}, (\text{noise} < 0) \end{cases} \quad (1)$$

The area used to estimate the average signals and noise on the footwall is outlined by a square, the length of which is equal to that of the fault plane (the red box in Figs 3b and e). This square box covers the footwall area with major deformation as shown in Fig. 5. The 'signal' could be: (1) > 0 for especially low dip angle and/or shallow fault position, as shown in Fig. 5; (2) < 0 and '|signal|'$<$ 'noise' and (3) < 0 and '|signal|' $>$ 'noise'. In the simulation using the medium noise level (Fig. 2b), the noise in the target areas is always positive, that means only the models with R < 0 can be uniquely determined since the subsidence signal in the foot wall has to be larger than the noise if the causative fault model can be uniquely determined.

Fig. 7 presents the domain in which the fault geometry cannot be accurately resolved by InSAR measurements. In Figs 7(q)–(r), we also show the relations between the numbers of earthquakes without ambiguous model parameters and their corresponding 'causative fault' strike/dips. We found: (1) the ambiguity strongly depends on the rupture depth and earthquake magnitude. At the medium noise level, it is impossible to uniquely determine the dip orientation of earthquakes with $M_w < 6.0$ and depth > 5.0 km, (2) the dip angles of the 'causative fault' are also important (Fig. 7r). The earthquakes with steeper fault planes are significantly easier to resolve since the steeper fault will create larger subsidence in the footwall (Figs 5a and b), and (3) the strike of the 'causative fault' matters (Fig. 7q). Earthquakes with near E–W strike orientations are more difficult to be determined since the compressional faulting results in more N–S displacement, which the InSAR technique is insensitive to.

The cases with ambiguous InSAR-based models, for example the 2008 M_w 6.3 Qaidam earthquake, the 2016 M_w 5.9 Menyuan earthquake, the 2016 M_w 6.3 Jinghe earthquake, rightly locate on zone between the positive and negative region in Fig. 7, which indicates these previous ambiguous models result from the subsidence signals close to the background noise level.

6 DISCUSSION

The exponential increase in the number of InSAR observations, along with the capacity of detecting small earthquakes, makes a geodetic earthquake catalogue possible in the near future

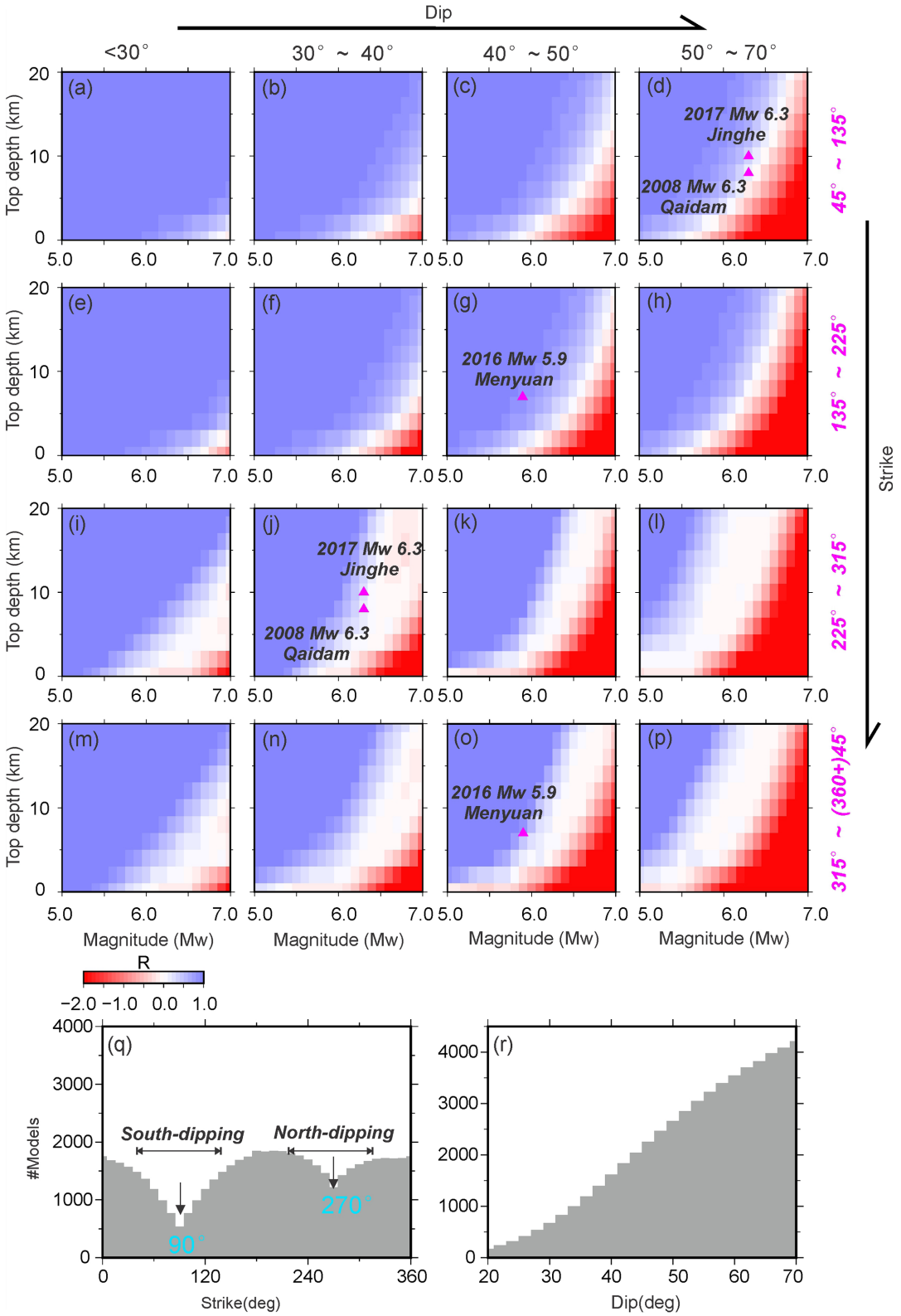

Figure 7. The domain of the ambiguous model parameters under the medium background noise level shown in Fig. 2(b). (a–p) The variations of the *R* value with the earthquake parameters (top-depth, dips, strike and magnitude). The pink triangles mark the real earthquakes with ambiguous parameters based on the nodal planes of focal mechanisms (Table S1). (q–r) the numbers of earthquakes as a function of strike and dip angle. The two panels only include the cases, the 'causative fault' parameters of which can be uniquely determined based on InSAR.

(Feng *et al.* 2015; Atzori *et al.* 2019). When SAR data are made available in near-real time, as with COSMO-SkyMed imagery during the 2009 L'Aquila earthquake (Central Italy), seismic source models can be continuously generated and updated during the seismic sequence (Salvi *et al.* 2009). In comparison to the conventional seismological earthquake catalogue, these geodetic earthquake catalogues provide a big database with an alternative, and sometimes more accurate source of earthquake source information (i.e. locations, dips, strike, rake, depth, moment) allowing us to revisit the tectonic and geology lessons we learned from seismological earthquake catalogues. That would be boosted by the big data and machine learning techniques (Bergen *et al.* 2019; Kong *et al.* 2019). However, determining the correct fault plane from InSAR data is still challenging. Here we highlight that the ambiguous fault geometry derived from InSAR measurements of buried thrust earthquakes should be seriously considered in the coming geodetic earthquake catalogue era.

Our work therefore benefits the emerging field of operational earthquake source modelers who want to automate the analysis of earthquake source inversion. We are able to give a threshold based on the 'R' value to determine if the automated result is reasonable in light of the data uncertainties, which can be used to flag if manual analysis is needed. The major cause of the apparent ambiguous fault geometry is the small SNR of the interferograms of particular earthquakes, and whether the subsidence signal on the footwall can be recognized from the noise is the key to determining the correct fault plane. Using the 'R' value could be helpful as a quick check for earthquake modelling if one can expect to be able to infer a unique fault plane geometry based on InSAR. Based on our strategy, a valuable work is to re-examine whether the past inferred fault models of smaller buried thrust earthquakes is reasonable.

We argued in Section 4 that we can uniquely determine the fault dip orientation from InSAR measurements as long as the SNR is large enough. In recent publications, several ambiguous fault models in small earthquakes have been successfully solved by using techniques of removing atmospheric noises, such as GACOS and Stacking InSAR (Ghayournajarkar & Fukushima 2020; Hou *et al.* 2020). The InSAR time-series analysis is also potentially being applied in the coseismic deformation extraction and could significantly improve interferogram quality (Daout *et al.* 2019, 2020).

With an increasing number of satellites and also the existence of multi-satellite constellations, such as the COSMO-SkyMed constellation of four satellites with a high resolution SAR and Sentinel-1A/B (Caltagirone *et al.* 2007; Salvi *et al.* 2012), the detection ability of space-based remote sensors is being enhanced, and their noise levels reduced, particularly for the satellites, which can have flexible viewing geometries, that is right-/left-looking (Morishita *et al.* 2016). With updated InSAR observations with high SNR in the near future, it may be possible to significantly reduce the ambiguity in fault geometry discussed in this paper.

Before the extensive InSAR observations with small SNR are available, combining multiple data sets, such as geodetic measurements, seismology, strong motion, precisely relocated aftershocks and geomorphology analysis, is an alternative way to help to determine a unique source fault geometry from the ambiguous source model parameters. The combination of multiple constraints has been widely accepted to rule out the ambiguous models in recent years, but it is hard to apply in big data analysis, since the availability, sensitivities and uncertainties associated with each data source are highly variable.

7 CONCLUSIONS

We performed kinematic slip inversions of synthetic data generated by combining GACOS atmospheric delays and white noise with synthetic thrust earthquake displacements. Our inversions quantitatively demonstrate the ambiguity of deriving ∼E–W striking thrust fault geometries from polar-orbiting SAR satellite measurements of ground deformation, in which two fault planes with opposing dips can fit the data equally well in the presence of atmospheric and random noise. The source fault ambiguity results from either the disappearance of subsidence in the footwall as the dip angle decreases and the depth increases, or the subsidence lobe moving to the hanging wall due to an unusual gentle dip angle. Fault models derived from inverting the synthetic data predict very similar 3-D surface deformation patterns with only subtle differences, indicating that the 1-D measurement of InSAR is not the main cause of the fault plane ambiguity. We suggest the main cause of the apparent ambiguous fault model is the small SNR in the fault foot wall. We proposed the simple 'R' value to quantify if the 'correct' fault plane can be resolved from the InSAR measurements. We then mapped out the distribution of the ambiguous models in the parameter domain, and found the occurrence of the fault plane ambiguity strongly relies on the dip, strike, rupture depth and earthquake magnitude (slip). At the natural atmospheric noise level in western China, it is hard to resolve this model ambiguity just based on the InSAR observations alone for the buried thrust earthquakes smaller than M_w 6.0. We highlight our method as a potential data driven way to determine if fault ambiguity can or cannot be ruled out based on InSAR data.

ACKNOWLEDGEMENTS

We thank the editor, Andreas Steinberg and one anonymous reviewer for their comments on the manuscript. We thank Dr Sam Wimpenny for his help in manuscript writing. The atmospheric delay data were downloaded from the Generic Atmospheric Correction Online Service for InSAR (GACOS) (http://www.gacos.net/). All figures were made using the Generic Mapping Tools software package v.4.5.9 (https://www.generic-mapping-tools.org/; Wessel and Smith, 1998). This work was funded by the National Natural Science Foundation of China (41631073) and the National Key Research and Development Program of China (No. 2018YFC1503602; No. 2019YFC1509205).

REFERENCES

Anderson, E.M., 1951. *The Dynamics of Faulting,* 2nd edn, Oliver & Boyd.

Ainscoe, E.A., Elliott, J.R., Copley, A., Craig, T.J., Li, T., Parsons, B.E. & Walker, R.T., 2017. Blind thrusting, surface folding, and the development of geological structure in the Mw 6.3 2015 Pishan (China) Earthquake, *J. geophys. Res.,* **122**(11), 9359–9382.

Atzori, S., Antonioli, A., Tolomei, C., Novellis, V., Luca, C. & Monterroso, F., 2019. InSAR full-resolution analysis of the 2017–2018 M>6 earthquakes in Mexico, *Remote Sens. Environ.,* **234,** 111461.

Barnhart, W.D., Brengman, C., Li, S. & Peterson, K., 2018. Ramp-flat basement structures of the Zagros Mountains inferred from co-seismic slip and afterslip of the 2017 Mw7.3 Darbandikhan, Iran/Iraq earthquake, *Earth planet. Sci. Lett.,* **496,** 96–107.

Beaumont, D., Scotti, O., Courboulex, F. & Melis, N., 2004. Complex kinematic rupture of the Mw 5.9, 1999 Athens earthquake as revealed by the joint inversion of regional seismological and SAR data, *Geophys. J. Int.,* **158,** 1078–1087.

Bergen, K., Johnson, P., Hoop, M. & Beroza, G., 2019. Machine learning for data-driven discovery in solid Earth geoscience, *Science,* **363,** 6433.

Bos, A.G., Usai, S. & Spakman, W., 2004. A joint analysis of GPS motions and InSAR to infer the coseismic surface deformation of the Izmit, Turkey earthquake, *Geophys. J. Int.,* **158,** 849–863.

Biggs, J., Wright, T., Lu, Z. & Parsons, B., 2007. Multi-interferogram method for measuring interseismic deformation: Denali Fault, Alaska, *Geophys. J. Int.,* **170,** 1165–1179.

Caltagirone, F., Angino, G., Impagnatiello, F., Capuzi, A., Fagioli, S. & Leonardi, R., (2007). COSMO-SkyMed: an advanced dual system for Earth observation, in *Proceedings of the Internationa Geoscience and Remote Sensing Symposium (IGARSS07),* Barcelona.

Copley, A.,Karasozen E.,Oveisi B.,Elliott J. &, Nissen E., 2015, Seismogenic faulting of the sedimentary sequence and laterally variable material properties in the Zagros Mountains (Iran) revealed by the August 2014 Murmuri (E. Dehloran) earthquake sequence.. , *Geophys. J. Int.,* **203,** 1436–1459.

Dawson &Tregoning, 2007. Uncertainty analysis of earthquake source parameters determined from InSAR: a simulation study, *J. geophys. Res.,* **112,** B09406, doi:10.1029/2007JB005209.

Daout, S., Sudhaus, H., Kausch, T., Steinberg, A. & Dini, B., 2019. Interseismic and postseismic shallow creep of the North Qaidam Thrust faults detected with a multitemporal InSAR analysis, *J. geophys. Res.,* **124,** doi:10.1029/2019JB017692.

Daout, S., Steinberg, A., Isken, M.P., Heimann, S. & Sudhaus, H., 2020. Illuminating the spatio-temporal evolution of the 2008–2009 Qaidam earthquake sequence with the joint use of insar time series and teleseismic data, *Remote Sensing,* **12**(17), 2850.

Elliott, J.R., Parsons, B., Jackson, J.A., Shan, X., Sloan, R.A. & Walker, R.T., 2011. Depth segmentation of the seismogenic continental crust: the 2008 and 2009 Qaidam earthquakes, *Geophys. Res. Lett.*, **38**(6), L06305, doi:10.1029/2011GL046897.

Elliott, J., Walters, R. & Wright, T., 2016. The role of space-based observation in understanding and responding to active tectonics and earthquakes, *Nat. Commun.,* **7,** 13844.

Farr, T.G. *et al.*, 2007. The shuttle radar topography mission, *Rev. Geophys.,* **45,** 2.

Ferretti, 2014. *Satellite InSAR Data – Reservoir Monitoring From Space,* EAGE Publications, ISBN-13: 978–9073834712.

Feng, G. & Jónsson, S., 2012. Shortcomings of InSAR for studying megathrust earthquakes: the case of the Mw9. 0 Tohoku-Oki earthquake, *Geophys. Res. Lett.,* **39,** L10305, doi:10.1029/2012GL051628.

Feng, L., Hill, E., Banerjee, P., Hermawan, I., Tsang, L., Natawidjaja, D., Suwargadi, B. & Sieh, K., 2015. A unified GPS-based earthquake catalog for the Sumatran plate boundary between 2002 and 2013, *J. geophys. Res.,* **120,** 3566–3598.

Ghayournajarkar &Fukushima, 2020. Determination of the dipping direction of a blind reverse fault from InSAR: case study on the 2017 Sefid Sang earthquake, northeastern Iran, *Earth, Planets Space,* **72,** 64.

Goldstein, R.M., 1995. Atmospheric limitations to repeat-track radar interferometry, *Geophys. Res. Lett.,* **22**(18), 2517–2520.

Gong, W.Y., Zhang, Y.F., Li, T., Wen, S.Y., Zhao, D.Z., Hou, L.Y. & Shan, X.J., (2019) Multi-sensor geodetic observations and modeling of the 2017 Mw 6.3 Jinghe earthquake, *Remote Sens.,* **11**(18), 2157.

Hanssen, R., 1998. Assessment of the role of Atmospheric heterogeneities in ERS Tandem SAR interferometry - Delft University Press, DEOS Report no 12698.1, 1998, Delft, the Netherlands., Assessment of the role of Atmospheric heterogeneities in ERS Tandem SAR interferometry - Delft University Press, DEOS Report no 12698.1, 1998, Delft, the Netherlands.

He, P. *et al.*, (2016). Source model of the 2015 Mw6.4 Pishan earthquake constrained by interferometric synthetic aperture radar and GPS: Insight into blind rupture in the western Kunlun Shan, *Geophys. Res. Lett.,* **43,** 1511–1519.

He, P., Wen, Y.M., Chen, Y.G., Xu, C.J. & Ding, K.H., (2020). Coseismic rupture geometry and slip rupture process during the 2018 Mw 7.1 Anchorage, South-Central Alaska Earthquake: intraplate normal faulting by slab tear constrained by geodetic and teleseismic data, *Earth Space Sci.,* **7,** 1.

Hou, L.Y., Shan, X.J., Gong, W.Y., Zhang, Y.F., Luo, H. & Zhao, D.Z, (2020). Characterizing seismogenic fault of 2016 Dingjie earthquake based on multitemporal DInSAR, *Chin. J. Geophys. (in Chinese),* **63**(4), 1357–1369.

Jackson, J.A. & White, N.J., (1989). Normal faulting in the upper continental crust: observations from regions of active extension, *J. Struct. Geol.,* **11,** 15–36.

Kong, Q., Trugman, D., Ross, Z., Bianco, M., Meade, B. & Gerstoft, P., (2019). Machine learning in seismology: turning data into Insights, *Seismol. Res. Lett.,* **90**(1), 3–14.

Konca, A. *et al.*, (2019). Slip distribution of the 2017 Mw6.6 Bodrum–Kos earthquake: resolving the ambiguity of fault geometry, *Geophys. J. Int.,* **219**(2), 911–923.

Yao, Y., Wen, S., Li, T. & Wang, C., (2020). The 2020 Mw 6.0 Jiashi earthquake: a fold earthquake event in the Southern Tian Shan, Northwest China, *Seismol. Res. Lett.,* doi:10.1785/0220200146.

Lohman, R.B. & Barnhart, W.D., (2010). Evaluation of earthquake triggering during the 2005–2008 earthquake sequence on Qeshm Island, Iran, *J. geophys. Res.,* **115,** B12413, doi:10.1029/2010JB007710.

Lohman, R.B., Simons, M. & Savage, B., (2002). Location and mechanism of the Little Skull Mountain earthquake as constrained by satellite radar interferometry and seismic waveform modeling, *J. geophys. Res.,* **107**(B6), 2118.

Middleton, T.A. & Copley, A., (2014). Constraining fault friction by reexamining earthquake nodal plane dips, *Geophys. J. Int.,* **196**(2), 671–680.

Massonnet, D. & Feigl, K., (1998). Radar interferometry and its application to changes in the Earth's surface, *Rev. Geophys.,* **36**(4), 441–500.

Massonnet, D., Feigl, K., Rossi, M. & Adragna, F., (1994). Radar interferometric mapping of deformation in the year after the Landers earthquake, *Nature,* **369**(6477), 227–230.

Morishita, Y., Kobayashi, T. & Yarai, H., (2016). Three-dimensional deformation mapping of a dike intrusion event in Sakurajima in 2015 by exploiting the rightand left-looking ALOS-2 InSAR, *Geophys. Res. Lett.,* **43,** 4197–4204.

Okada, Y., (1985). Surface deformation due to shear and tensile faults in a half-space, *Bull. seism. Soc. Am.* **75**(4), 1135–1154

Salvi, S., Vignoli, S., Serra, M. & Bosi, V., (2009). Use of Cosmo-Skymed data for seismic risk management in the framework of the ASI-SIGRIS project, in *Proceedings Geoscience and Remote Sensing Symposium.,* IGARSS,pp. II–921-II-924, doi:10.1109/IGARSS.2009.5418248.

Salvi, S., Stramondo, S., Funning, G.J., Ferretti, A., Sarti, F. & Mouratidis, A., (2012). The Sentinel-1 mission for the improvement of the scientific understanding and the operational monitoring of the seismic cycle, *Rem. Sens. Environ.,* **120**(15), 164–174.

Sloan, R.A., Jackson, J.A., McKenzie, D. & Priestley, K., (2011). Earthquake depth distributions in central Asia, and their relations with lithosphere thickness, shortening and extension, *Geophys. J. Int.,* **189,** 1–29.

Sibson, R.H. & Xie, G., (1998). Dip range for intracontinental reverse fault ruptures: truth not stranger than fiction? *Bull. seism. Soc. Am.,* **88,** 1014–1022.

Steck, L.K., Phillips, W.S., Mackey, K., Begnaud, M.L., Stead, R.J. & Rowe, C.A., (2009). Seismic tomography of crustal P and S across Eurasia, *Geophys. J. Int.,* **177**(1), 81–92.

Wang, R., Diao, F. & Hoechner, A., (2013). SDM—a geodetic inversion code incorporating with layered crust structure and curved fault geometry, in *Paper Presented at 2013 EGU General Assembly Conference*, Vienna, Austria

Wang, H. *et al.*, (2017). Sentinel-1 observations of the 2016 Menyuan earthquake: a buried reverse event linked to the left-lateral Haiyuan fault, *Int. J. Appl. Earth Obs. Geoinf.,* **61,** 14–21.

Wei, S.Q. *et al.*, (2010). Regional earthquakes in northern Tibetan Plateau: implications for lithospheric strength in Tibet, *Geophys. Res. Lett.* **37,** L19307, doi:10.1029/2010GL044800.

Wright, T.J., Parsons, B.E. & Lu, Z., (2004). Toward mapping surface deformation in three dimensions using InSAR, *Geophys. Res. Lett.,* **31**(1), doi:10.1029/2003GL018827.

Yu, C., Li, Z., Penna, N.T. & Crippa, P., (2018). Generic atmospheric correction model for Interferometric Synthetic Aperture Radar observations, *J. geophys. Res.,* **123,** doi:10.1029/2017JB015305.

Zebker, H., Rosen, P. & Hensley, S., (1997). Atmospheric effects in interferometric synthetic aperture radar surface deformation and topographic maps, *J. geophys. Res.,* **102,** 7547–7563.

Zhang, Y.F., Shan, X.J., Zhang, G.H., Zhong, M.J., Zhao, Y.J., Wen, S.Y., Qu, C.Y. & Zhao, D.Z., (2020). The 2016 Mw 5.9 Menyuan Earthquake in the Qilian Orogen, China: a potentially delayed depth-segmented rupture following from the 1986 Mw 6.0 Menyuan Earthquake, *Seismol. Res. Lett.,* **91**(2A), 758–769.

Zhang, G., Hetland, E. & Shan, X., (2015). Slip in the 2015 Mw 7.9 Gorkha and Mw 7.3 Kodari, Nepal, earthquakes revealed by seismic and geodetic data: delayed slip in the Gorkha and slip deficit between the two earthquakes, *Seismol. Res. Lett.,* **86**(6), 1578–1586.

SUPPORTING INFORMATION

Supplementary data are available at *GJI* online.

R_code.zip
Supporting-Information.doc

Please note: Oxford University Press is not responsible for the content or functionality of any supporting materials supplied by the authors. Any queries (other than missing material) should be directed to the corresponding author for the paper.